Journal of Wind Engineering & Industrial Aerodynamics 209 (2021) 104463

Contents lists available at ScienceDirect

Journal of Wind Engineering & Industrial Aerodynamics

journal homepage: www.elsevier.com/locate/jweia

A field study on the aerodynamics of freight trains

Ariq Quazi [a,*], Timothy Crouch [a], James Bell [a,c], Tony McGreevy [b], Mark C. Thompson [a], David Burton [a]

[a] Department of Mechanical and Aerospace Engineering, PO Box 31, Monash University, 3800, Australia
[b] Pacific National, Melbourne, Victoria, Australia
[c] German Aerospace Center (DLR), Institute for Aerodynamics and Flow Technology (AS), Göttingen, Germany

ARTICLE INFO

Keywords:
Train aerodynamics
Bluff bodies
Field measurement
Aerodynamic drag
Experimental methods

ABSTRACT

A novel full-scale field test was undertaken to assess the aerodynamic performance of shipping containers loaded on inter-modal freight trains. The aerodynamic performance of an instrumented 48 ft container, located 185 m downstream of the locomotive, is assessed in the context of surface pressure, weather station, and GPS data sets. Previous studies on the aerodynamics of trains have been largely limited to low-resolution, reduced-order and scaled; field, numerical and wind-tunnel studies; respectively. The objective here was to determine the capacity of this novel field-based method to assess the aerodynamic performance of full-scale train containers for a large range of operating conditions. For low wind conditions, where the yaw angle is predicted to be low, measured surface pressure distributions on the front and base of the container are similar to that of past work however the magnitude of the drag coefficient was much lower, by up to 65%. This suggests that previous studies are yet to fully detail the drag profile of containers located at large downstream distance. Observed asymmetry of the pressure distribution on the front of the container are generally consistent with wind conditions measured at nearby weather stations and can be used as a proxy to determine the wind yaw angle at the train.

1. Introduction

Diesel-powered locomotives remain one of the most favoured means of hauling freight by trains over long distances. Reducing fuel consumption of existing freight trains by better understanding the resistances that need to be overcome has never been more relevant. One source of energy loss, the aerodynamic resistance (drag), has not had the same research focus when compared to other vehicles, such as cars and high speed trains. This may be in part due to an inaccurate perception that inter-modal freight trains travel at low speeds, where the aerodynamic resistance force follows a quadratic trend with velocity, as given by the well known Davis equation (Davis, 1926). In fact, speeds of up to 110 km/h are common on many railways with the potential of faster speeds in the future, including within Australia where transcontinental journeys are frequent.

Inter-modal freight trains transport different combinations of freight. It is typical that two or more locomotives haul the freight, which can be made up of standardised containers (although of varying heights and lengths) and non-standardised cargo. The rolling stock also varies in type, length and height (e.g., well and flat wagons); containers can be single or double-stacked; and empty slots may exist. The lack of a slot being utilised is an outcome of sets of multiple wagons being grouped together where certain container sizes do not fit or are not required. Any given train will have a unique geometry. Hence, the aerodynamic flows exhibit different characteristics depending on the dimensions of the containers or cargo, and how they are loaded onto the wagons (Gielow and Furlong, 1988; Watkins et al., 1992; Soper et al., 2014; Li et al., 2017; Maleki et al., 2019). Another key variable is the length of the train and how the boundary layer forms around the train, noting that freight trains can extend beyond 1.6 km in length (Bell et al., 2020).

Typically, aerodynamic properties of the train are taken away from the ideal conditions by other constraints. Rather, these trains are loaded according to an algorithm that takes into account the distribution of mass, the axle weight loads, and slot efficiency along the length of the train. A need exists to better understand the complex aerodynamics of these trains and to determine how the freight can be best loaded in the most aerodynamic manner. An attempt at achieving this was made in Lai et al. (2008) where the drag associated with every gap was determined analytically by an exponential model from the work carried out in Engdahl et al. (1987) and Gielow and Furlong (1988). For a sample route, the

* Corresponding author.
E-mail address: ariq.quazi@monash.edu (A. Quazi).

https://doi.org/10.1016/j.jweia.2020.104463
Received 1 July 2020; Received in revised form 26 October 2020; Accepted 23 November 2020
Available online 23 December 2020
0167-6105/© 2020 Elsevier Ltd. All rights reserved.

study found the reduction in drag by optimising the gap spacing contributed to a saving of 15 million gallons of fuel per year. However, the mathematical model did not take into account the presence of large gaps where an empty slot is present and also did not consider double-stacked containers.

The common approach for studying the aerodynamics of trains include wind-tunnel tests (Gielow and Furlong, 1988; Watkins et al., 1992; Golovanevskiy et al., 2012; Li et al., 2017; Giappino et al., 2018), numerical simulations (Flynn et al., 2014; Östh and Krajnović, 2014; Uystepruyst and Krajnović, 2013; Maleki et al., 2017, 2019), moving scale model tests (Soper et al., 2014, 2015), track-side testing (Sterling et al., 2008; Bell et al., 2020; Baker et al., 2014), and on train full-scale testing (Gallagher et al., 2018). However, to the authors' knowledge no studies have been carried out investigating the pressures seen on an inter-model container loaded in standard operational positions along the train. This is important since modelling a full-scale freight train, which can have length to height ratios (L/H) between 250 and 500, becomes difficult as wind tunnels are restricted by their physical limits and numerical simulations exceed available computation resources. Applying a periodic boundary condition during simulations can partially offset these challenges (Östh and Krajnović, 2014) where it was found that the drag in the 'middle' section of the train was 90% lower than the leading locomotive. Moving-model setups have also been used (Soper et al. (2014)); however, the length of the train is still restricted by the length of the facility.

1.1. Aerodynamics at zero yaw conditions

The initial consideration of freight train aerodynamics is the behaviour of a container in free-stream conditions where it is not influenced by other containers or geometries. The oncoming flow impinges on the front surface creating a region of high pressure, and separates at the side and roof windward edges. The separated shear layers then reattaches over the length of the container. This phenomenon was shown by Taylor et al. (2011) for a two-dimensional elongated bluff body with a length-to-height ratio of 7:1 and later by Östh and Krajnović (2014) for a three-dimensional representative wagon and container, with length to width ratio of 5:1. Further, Li et al. (2015) and Maleki et al. (2017) concluded that similar features were evident for a double-stacked configuration through wind tunnel and numerical experiments respectively.

On the base surface two asymmetric wake vortices in the span-wise plane have been observed, with the core of the lower vortex closer to the face of the container (Östh and Krajnović, 2014; Uystepruyst and Krajnović, 2013; Maleki et al., 2019). This is caused by the air losing momentum as it interacts with the detailed wagon features below the container. The core of the higher vortex was seen to be further downstream due to higher velocity of flow over the top of the container. A ring vortex is also observed which is formed by the four separating shear layers off the trailing edges and combining together.

Under operational conditions the pressure drag associated with a container in a freight train is a function of the gap size upstream and downstream of the container, with the front gap having a dominant effect (Li et al., 2017; Maleki et al., 2019). As the gap size increases the drag coefficient continues to increase until a gap size of $9.46W$ in Li et al. (2017) and after a gap size of $5.76W$ in Maleki et al. (2017), after-which it plateaus and remains stable. The effect of having an empty slot directly upstream of the test container, where a single 40-foot container was absent in a 6-car model at was investigated by Gielow and Furlong (1988), who found that the difference in drag-area between having a complete single-stacked train and missing one container was ~ 13.3 ft^2 (C_D of 0.175).

Estimates of the change in slipstream boundary layer development with respect to distance from the front of train have been provided for freight trains by Soper et al. (2014) and Bell et al. (2020). Together, these indicated that the boundary layer stabilises after some distance in zero cross-wind. The change in drag experienced by a container along the length of the train was investigated by Engdahl et al. (1987) where a full-scale gondola wagon was instrumented with a force balance and placed on a train between the 2nd to the 30th wagon position. It was found that after the eighth position (160 m) the force on the instrumented wagon remained stable, being approximately 30% of the second position. Other studies, Watkins et al. (1992), Engdahl et al. (1987) and Golovanevskiy et al. (2012), have found similar trends but for different train lengths.

1.2. Effect of cross-winds

A train operating in a field environment will be exposed to natural tail, head and cross-winds, which will change the nature of the flow over individual containers. Cross-winds are of particular importance to train aerodynamics, in terms of stability. Extensive research has been carried out in this area to characterise the flow topology (Copley, 1987; Baker et al., 2014; Baker, 2010; Baker and Sterling, 2009; Hemida and Krajnović, 2010; Krajnović et al., 2012). However, the effect of the aerodynamic drag is also of importance. Watkins et al. (1992) investigated the effect of cross-wind for a scale model train where the wagon at the centre was deemed to be representative of the 'middle' section of a full-scale train. A quadratic relationship between the increase in the drag coefficient and the yaw angle was seen for yaw angles up to 15°. A similar trend was also later seen by Golovanevskiy et al. (2012) to exist over a similar range. Further, studies such as Beagles and Fletcher (2013); Giappino et al. (2018); Maleki et al. (2020) have looked at the effect on the pressure drag coefficient. They found that over a range of yaw angles about zero, a quadratic trend in the drag was observed, but beyond ~30° the drag starts to decrease.

A moving-model test undertaken by Soper et al. (2015) analysed a 4-wagon consist with one lead vehicle, at a yaw angle of 30°. One container was pressure-tapped and three different loading configurations tested. Increasing the gap in front of the instrumented container was seen to cause the largest differences in drag coefficients. The highest magnitudes of pressure on the front face was seen on the windward edge, associated with the impinging cross-wind. A pressure gradient from positive to negative persisted, suggesting a suction of air from the gap. The base face is characterised by a region of negative pressure where a smaller rear gap resulted in a large degree of asymmetry in the distribution. This was explained to be due to the flow accelerating through the smaller gap. For a larger gap size the distribution is seen to be relatively uniform.

Flynn et al. (2016) undertook numerical simulations of the same test set up as Soper et al. (2015) with the train fully loaded to determine the effect of the slipstream. It was found that higher velocities persisted on the leeward side than the windward side. Maleki et al. (2020) who investigated the effect of cross-wind over a range of gap sizes explained this phenomenon to be due to the unsteady longitudinal vortex originating at the windward corner of the roof, creating a region of low pressure along the leeward face. Bell et al. (2020) found through full-scale track side testing of the boundary layer that yaw angles of 2° and larger pushed the boundary layer to be biased to one side of the train.

1.3. Aim

Field data on the boundary layer development along operational freight trains have been provided by Sterling et al. (2008) and Bell et al. (2020) and full scale force and pressure results have been given be Engdahl et al. (1987) and Gallagher et al. (2018). There have also been successful field pressure measurements of other vehicles and structures. For example, Surry (1991) and Richardson et al. (1997) investigated the pressures on a full-scale building and Quinn et al. (2007) conducted testing on a commercial vehicle at full-scale analysing the induced rolling moment. These studies are important as they provide validation of scale-model experiments in wind tunnels and numerical simulations.

Despite this, there remains limited available experimental data that describes the drag experienced by trains in the field. The reason for this is likely due to the difficulty in obtaining such data as it requires a complex set-up and considerable logistics to implement. As such, no detailed field data is available to directly correlate the wind tunnel and numerical studies in the natural environment, with the detailed train geometry, correct length and at representative Reynolds numbers.

Hence, this study aims to describe a method and present results from on-board container pressure measurements, and to better understand full-scale container surface pressure distributions for comparison with other recent experiments and simulations. Given the nature of the environment and a number of uncontrolled variables, a number of steps are taken to justify the validity of the data that was obtained. A detailed uncertainty analysis is undertaken. This is followed by determining the wind speed, wind direction and altitude obtained from remote weather stations to indicate the general climatic conditions and relating it to observations in the surface pressure distributions. To the authors' knowledge this is the first time a full-scale shipping container has been instrumented in such a manner. This work is in collaboration with Pacific National – a freight transport provider within Australia – with the ultimate aim of reducing the fuel consumption of freight trains by optimising the loading of different freight types to improve the aerodynamics.

2. Methodology

This section describes the on-board instrumentation, Data Acquisition Systems (DAS) and approach used to obtain container front and base pressure distributions. Experiments were conducted on a single-stacked freight train during one leg of a transcontinental journey across Australia. A detailed uncertainty analysis is presented so that the level of confidence in reported values may be assessed.

2.1. Instrumented container & pressure measurement system

Fig. 1 shows an image of the 48-foot refrigeration container that was instrumented with the on-board DAS and pressure transducers. It was selected for this study as it is a commonly used container and compared to other geometries it has relatively smooth side walls. This class of container was preferred as it provides a good comparison with the more simplified generic geometries typically employed by past wind tunnel and numerical studies (Li et al. (2017); Maleki et al. (2017)). With the outside refrigeration unit removed for this study the overall dimensions of the container measured 13.50 m (length), 2.44 m (width) and 2.90 m (height).

A schematic of the instrumented container, detailing the on-board instrumentation, is shown in Fig. 2. The front and base faces of the container are each pressure tapped with an array of 59 taps. The taps were evenly distributed over the faces apart from the edges where the density of the taps were increased to better resolve expected high pressure gradients. Custom made pressure manifolds were inserted into the front and base faces of the container. The pressure manifolds were CNC machined from solid brass stock to ensure the dimensions were consistent across all manufactured components. A schematic of the manifold is presented in Fig. 2, it consisted of a 5 mm internal diameter (ID) tube that tapers down to a 1.2 mm ID tube section. PVC tubing, of 1.2 mm ID and 3000 mm in length, connected the pressure manifolds to the differential pressure transducers housed within the instrumentation boxes. The front end of the pressure manifold had a flange that sat flush against the outside face of the container. A wire-mesh was placed over the flange to prevent large particles and insects from entering the manifolds. Wind tunnel testing on the manifolds with and without the wire-mesh screens attached was conducted to assess the influence of the wire mesh on the mean and unsteady pressure response. It was concluded that the wire mesh had no significant impact on the container surface pressure measurements.

The pressure taps were connected to four individual Dynamic Pressure Measurement (DPM) modules (two at each end). Turbulent Flow Instrumentation was the manufacturer of the pressure modules, which have a measurement range of ±2.5 kPa. Over the temperature range between 0°C–50 °C the manufacturer states the accuracy of the pressure measurements to be ±0.3% at full-scale, or ±7.5 Pa (ξ_{DPM}). Immediately prior to container experiments each pressure module was calibrated across a range of ±2 kPa, using a peristaltic pump to apply a known pressure. A Betz Manometer served as the reference pressure measurement device. All modules were found to be within the manufacturer's specification. During train experiments each DPM module was referenced to a plenum located inside the instrumentation boxes. The plenum was a well sealed plastic container. As a cross-check two reference pressure tubes were located free inside the container, one at either end. Over the course of the journey the standard deviation of the pressure inside the container was 7.5 Pa which corresponds to a drag coefficient of 0.014 at a train velocity of 60 km/h. A pitot-static tube, or similar reference devices located outside the container, could not be used to determine a free-stream reference pressure due to operational limitations which prevented any significant external protrusions from the container.

All four modules were connected to an on-board PC with an Ethernet connection. The PC was accessed remotely over the duration of the experiments via a 3G connection. On the base end of the container instrumentation box 1 housed two DPM modules, an Ethernet switch and the data acquisition (DAQ) modules. In each box the pressure modules and DAQ systems were fixed to a steel plate that sat on rubber vibration isolating legs. The instrumentation boxes were placed on a 1 m high frame to ensure the length of the PVC tubes were all the same and kept to a minimum. On the opposite end of the container two smaller cargo boxes (instrumentation box 2 and 3), each housed a DPM and a DAQ module. A GPS antenna was mounted outside on the door which provided data on the speed, altitude and location of the train. The instrumentation was powered by four 12 V absorbed glass gel mat batteries that also sat on a vibration isolating frame. This battery class was selected as it satisfied the operational safety requirements of hauling freight by the operator. On the outer side face of the container a 240 V power inlet plug was installed enabling the batteries to be charged at train depots without having to

Fig. 1. Instrumented 48 ft refrigeration shipping container (white, front) on board an operational freight train with significantly flatter external ridges than conventional containers (green, back). (For interpretation of the references to colour in this figure legend, the reader is referred to the Web version of this article.)

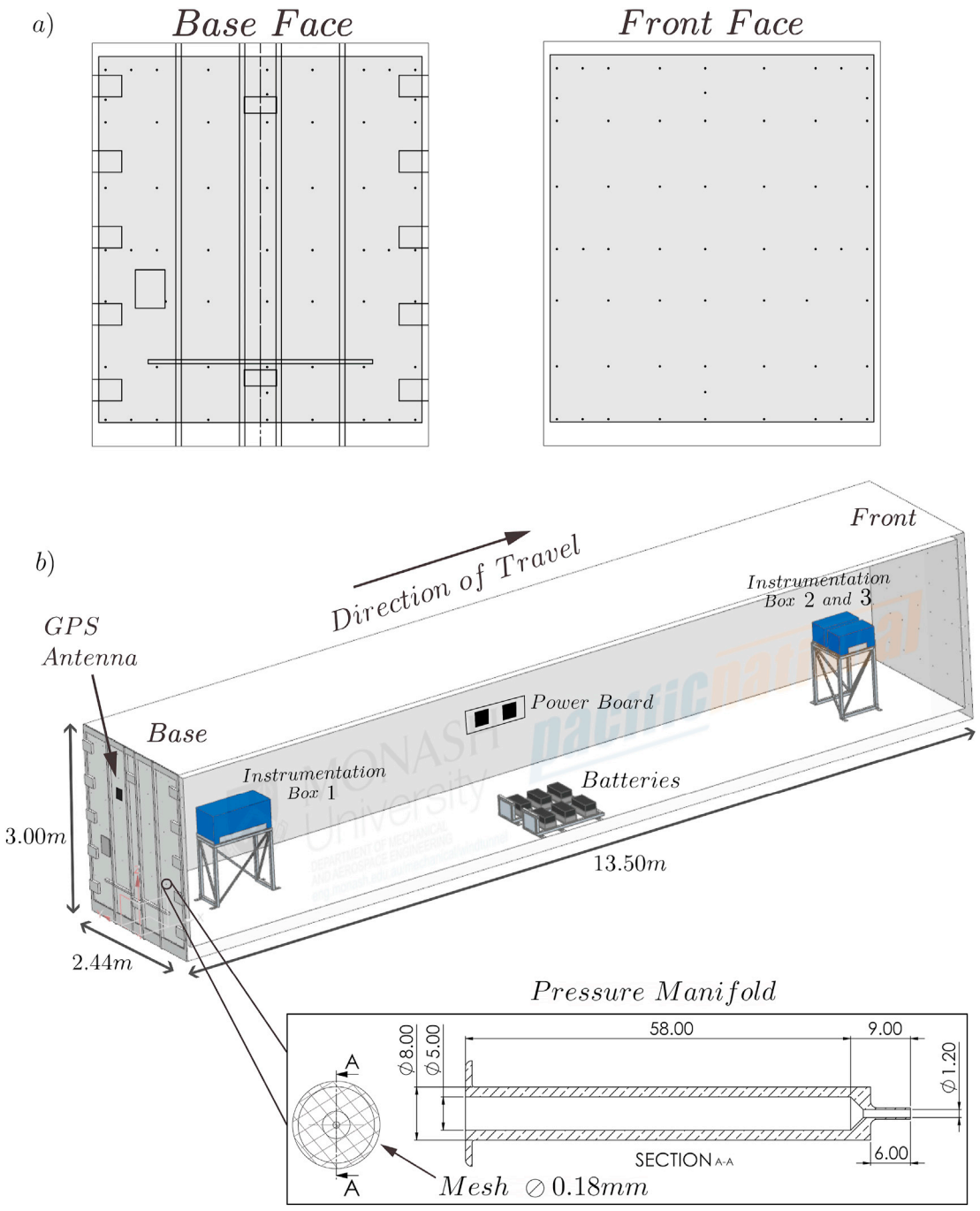

Fig. 2. a): Array of pressure taps on the front and base face where the shaded area represents the region over which pressure distributions have been interpolated. b): Instrumentation set up within shipping container including a schematic of the pressure manifold.

remove them from the container. The charging system electronics were configured such that while charging the batteries, the power to all the electronics were disconnected. This provided protection for the instrumentation in the event of current surges.

To conserve battery charge during transcontinental trips, a range of software features were implemented using a LabView interface. On disconnecting the batteries from mains power, the PC was configured to automatically turn on and remain in a low-power mode. In this mode, power was not supplied to the DPM and DAQ card interfaces. The high-power mode was triggered when the GPS signal recorded that the train had been travelling at speed >10 km/h for more than 15 min, at which point power was supplied to all instruments and DAQ systems and data recording commenced. Pressure and GPS data was logged at a rate of 1 Hz. Throughout a trip if the train maintained a speed <10 km/h for more than 15 min the system would automatically enter into the low-power mode. The on board PC had an in-built 3G sim card which enabled it to be accessed remotely. To track the train over the course of the trip, the system was configured to send out an email with its GPS coordinates, train speed and battery voltage every hour. In this way system health checks could be regularly performed throughout a trip and measures taken to rectify any data logging issues. There were some regions where the 3G signal was not consistent, however, for the majority of the trip the signal was found to be reliable.

2.2. Train loading configuration

The overall length of the test train was 1.3 km, and consisted of two locomotives and 194 20-foot container slots. Fig. 3 depicts the detailed stacking configuration of the train over first ~ 300 m. The instrumented container was positioned ~ 185 m from the nose of the train in the 28–29th slot, with 2 locomotives and 6 containers ahead of it, all single-stacked. Four empty slots existed both immediately upstream and downstream of the instrumented container. This equates to a gap size of 33.1 m or 13.6W, where 'W' is the width of the container, either side of the instrumented container.

The test configuration was carefully considered such that the instrumented container would be expected to lie outside of high pressure gradient regions with respect to changes in the drag coefficient with loading position along the length of the train and the upstream and downstream gap size. High gradient regions of the drag coefficient with loading position have been reported to exist over approximately the first 160 m of a freight train (Engdahl et al., 1987). Studies by Li et al. (2017) and Maleki et al. (2019) suggest that changes in container drag coefficient are low for upstream and downstream gap sizes $> 9.38W$ and $>5.76W$ respectively. Hence, based on previous studies, the loading position of the instrumented container is expected to lie within, or very close too, a relatively low drag coefficient gradient region with respect to both position along the train and the gap sizes at both ends of the container.

2.3. Test track and weather conditions

The path taken by the train is shown in Fig. 4. The instrumented container was loaded onto a train at Adelaide and travelled to Melbourne, which is one section of the transcontinental line between Perth and Melbourne, Australia. The distance of the trip was approximately 730 km. The train departed at midnight and arrived ~ 9 h later. During the trip the train speed remained above 100 km/h for ~ 3.2 h, and above 80 km/h for ~ 5.4 h. From Adelaide to near the Victorian border the altitude remains low at around 25 m with the general terrain being relatively flat. The gradient then steadily increases towards the Grampians (approximately 4.5 h into the journey) where the height above sea level peaks at 340 m. Coming into Melbourne the altitude decreases back to 25 m above sea level.

The locations of a number of Australian Bureau of Meteorology (BoM) weather stations in proximity to the track are also shown in Fig. 4. Weather station data was used to estimate the local temperature, mean sea level pressure (MSLP), humidity and wind conditions at the train during the trip. The average air temperature (T) during the trip was 21 °C, with a maximum of 25 °C and a minimum of 15 °C. The MSLP varied between 1.020 and 1.021 kPa. For selected track sections, numbered 1–5, the time-averaged wind speed and direction, recorded from nearby weather stations, are depicted in Fig. 4 for the period of time taken for the train to traverse each section. At the start of the trip a low westerly wind is present, however, throughout the course of the journey this fluctuated around to a southerly wind direction as a result of a low pressure trough moving through the region from a south westerly direction. The time-averaged wind speed measured throughout all track sections was ~ 8.3 km/h. Further details of the nature of the wind conditions present over the duration of the trip is provided in the results section.

The MSLP, P_{msl}, was corrected for altitude to determine the absolute atmospheric pressure at the weather station. The absolute atmospheric pressure was only taken for dry air, P_{atm}, as the moist air component accounted for <1% of the total pressure. Hence, P_{atm} and air density, ρ, are defined as:

$$P_{atm} = P_{msl} + \rho_{msl} \cdot g \cdot h, \tag{1}$$

and

$$\rho = \frac{P_{atm}}{R_{Dspec} \cdot (T + 273.15)}, \tag{2}$$

where ρ_{msl} is the air density at sea level (1.2 kg/m^3), h is the height above sea level in meters, g is gravity (9.8 m/s^2), R_{Dspec} is the specific gas constant of dry air and T is the temperature in degrees Celsius.

2.4. Stationary train reference measurements

The nature of the wider test program, consisting of multiple trips that were separately programmed, meant that for extended periods of time, sometimes weeks, the researchers did not have physical access to the system. As such, an important consideration in this type of test is the medium-term stability of the measurement, which is defined as the instrumentation drift over the duration of one leg in the transcontinental journey (in this case Adelaide to Melbourne). We consider this to be different to instrumentation drift between trips (long-term stability). In many other experimental environments, such as during wind tunnel testing, the period between zeroing instrumentation is short and can be controlled. Here the total trip duration was near 9 h, therefore the medium-term stability is taken as a source of uncertainty separate to that specified by the manufacture. To quantify this instrumentation drift an in-house lab test was undertaken where each DPM module was logged with no pressure applied over 12 h on four separate occasions. The average of the maximum deviation of all channels was determined to be 2.3 Pa. Medium-term stability, was determined to be within bounds that did not significantly affect the results, however, the long-term stability (i.e. between trips) was not.

During the trip, for operational reasons, the train came to a complete stop twice. As such, four stationary 'zero' measurements of 10 min were taken: before departing, during the two operational stoppages and after arrival. The four 'zero' samples were averaged to determine a new 'zero' and used to correct the data for the entire trip. Data recorded while the container is stationary will be subjected to the prevailing natural winds and associated pressures hence are not true 'zero' measurements. Given this limitation a general insight into the stability of the system can be made. The average of the absolute difference across all channels between the in-house lab zero testing and the four stationary 'zero' tests was determined to be < 3 Pa. The average of the maximum difference

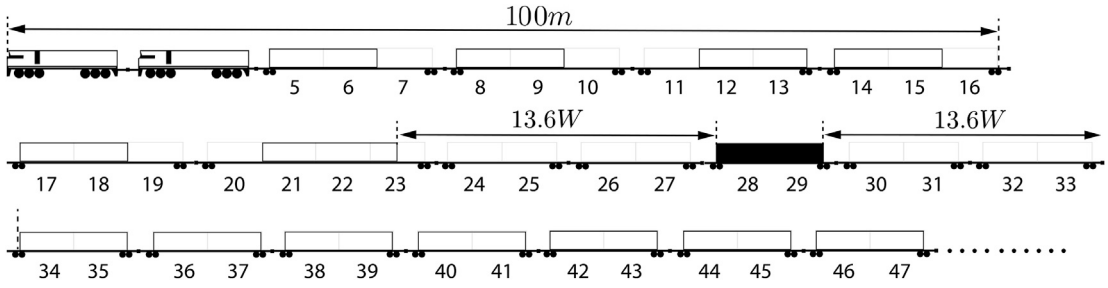

Fig. 3. Loading configuration of the first 300 m of the train. Where the first two vehicles are locomotives and treated as 2 container slots each. The instrumented container (black) is located 185 m from the front of the train.

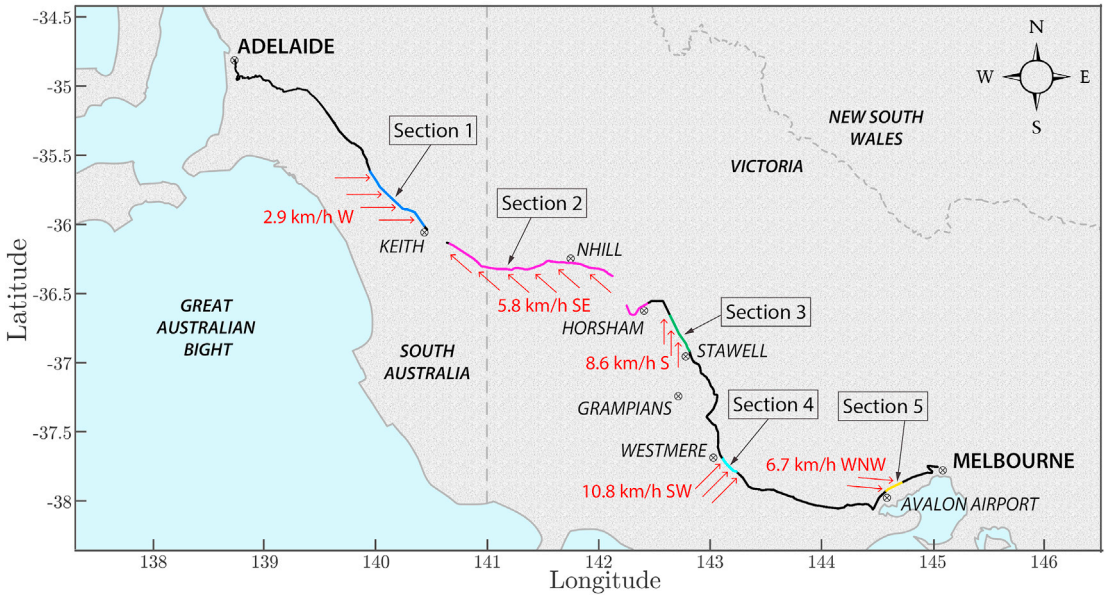

Fig. 4. Path taken by the train starting in Adelaide and finishing at Melbourne. The ⊗ markers are weather stations. Time-averaged wind speeds and directions over selected track sections are also shown. ● - Track section 1, ● - Track section 2, ● - Track section 3, ● - Track section 4, ● - Track section 5.

observed for any one of the four stationary 'zeros' for each channel relative to the lab conditions was <5 Pa, an order of magnitude lower than the pressure variation experienced by the container during operation. However, when expressed as a relative percentage of the magnitude of some of the surface pressures recorded, particularly on the base of the container, the long-term suitability of the transducers were found to be of significance. As such, the in-house zero was not used to correct the data. An example of a stationary 'zero' pressure coefficient distribution is plotted in Fig. 5. This figure reveals a largely random unbiased distribution, hence minimal effect of any ambient wind being present. This was also observed across all stationary 'zero' samples recorded throughout the trip. At the time of this recording, the weather station at Adelaide, located 8 km from the train, recorded a mean hourly wind speed of 13 km/h at a height of 10 m. This is consistent with the container experiencing a low-wind speed during the sample.

2.5. Uncertainty estimates

A characterisation of the uncertainty of the pressure coefficients are presented in this section. The uncertainty presented considers both accuracy and precision, which are combined by the root-sum-of-squares method (Holman, 2012). The uncertainty is described with reference to a train velocity, V_T, of 100 km/h, an air density of 1.2 kg/m^3 and a reference container surface pressure coefficient, $C_{p,ref}$, of 0.45 for a

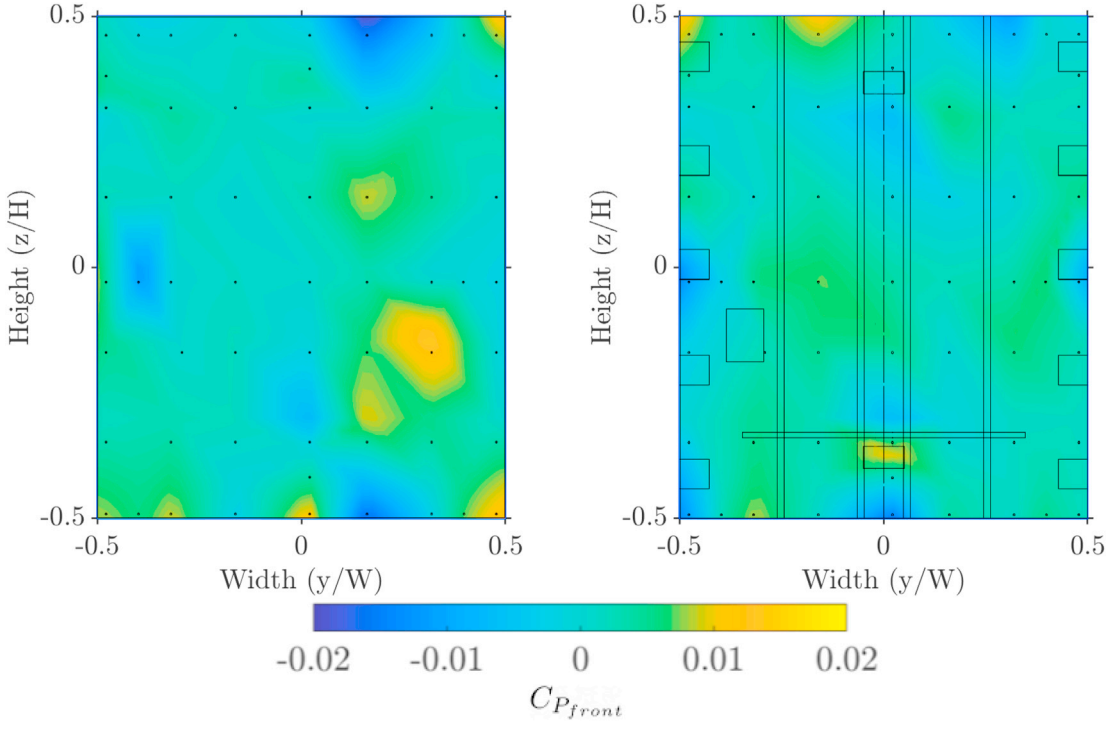

Fig. 5. Reference measurement of the front and base surface pressure contours taken when the train was stationary before departing Adelaide.

measured surface pressure of P. The pressure coefficients are dependent on the pressure measurement, air density and velocity. The sources of uncertainty considered for the measured pressure are summarised in Table 1. The primary source of system measurement uncertainty is associated with each DPM module, ξ_{DPM}, with secondary contributions associated with the calibration,$\xi_{calibration}$, and the medium- and long-term stability, $\xi_{med.stability}$, and $\xi_{long.stability}$. The accuracy of the data acquisition card, ξ_{DAQ}, is significantly better than the pressure transducers and has a negligible contribution to the overall uncertainty. Hence $\xi_{pressure}$ is defined as:

$$\xi_{pressure} = \sqrt{\xi_{DPM}^2 + \xi_{DAQ}^2 + \xi_{calibration}^2 + \xi_{med.stability}^2 + \xi_{long.stability}^2}, \quad (3)$$

where the combined uncertainty of the measured pressure was ±9.7 Pa. Density has been determined using a perfect gas assumption with inputs from temperature and atmospheric pressure, P_{atm}, as shown previously. All of which have been calculated from data obtained remotely from the nearest weather stations. The uncertainty associated with the MSLP, ξ_{msl}, is < 0.001 kPa and is not a primary source of uncertainty in reported pressure coefficients. The contribution of the change in altitude, $\xi_{altitude}$, to the uncertainty in air density has been considered. The train altitude was determined along the track from GPS data and the associated uncertainty has conservatively been taken to be ±10 m. The resulting uncertainty in the atmospheric pressure, ξ_{Patm}, due to $\xi_{altitude}$ was determined to be ±118 Pa. It was found that temperature measurements inside the container were not representative of the external conditions and obtaining external air temperature measurements was not possible due to mounting limitations and convective heat transfer interference from the external surfaces of the steel container. As a result the weather station data provided the best estimate of the local temperature at the train. Given the coarse distribution of weather stations along the length of the track the uncertainty in the temperature is estimated to be ±3 °C, ξ_{temp}. Taking these sources of uncertainty into consideration the combined uncertainty in the density, $\xi_{density}$, was evaluated at an altitude of 100 m from sea level and at a mean temperature of 21 °C by:

$$\frac{\xi_{density}}{\rho} = \sqrt{\left(\frac{\xi_{Patm}}{P_{atm}}\right)^2 + \left(\frac{\xi_{temp}}{T}\right)^2}, \quad (4)$$

and resulted in a total uncertainty of ±5.3%. The change in altitude had the largest impact followed by temperature and the mean sea level pressure. The train velocity is determined from the on board GPS which the manufacturer specifies to have an accuracy of ±0.1 km/h ξ_{speed} at 100 km/h (ublox, 2012). Hence, the combined fractional uncertainty in the reported pressure coefficient, ξ_{C_P}, is determined to be ±7.0%:

$$\frac{\xi_{C_P}}{C_{P,ref}} = \sqrt{\left(\frac{\xi_{pressure}}{P}\right)^2 + \left(\frac{\xi_{density}}{\rho}\right)^2 + \left(\frac{2 \cdot \xi_{speed}}{V_T}\right)^2}. \quad (5)$$

Table 1
Summary of uncertainties in measurements. The estimated source refers to an uncertainty associated with the remote location of the weather station with respect to the track.

Parameter	Uncertainty (±)	Source
ξ_{DPM}	7.5 Pa	TFI DPMS
ξ_{DAQ}	0.018 Pa	NI DAQ
$\xi_{calibration}$	4.9 Pa	Betz Manometer
$\xi_{med.stability}$	2.3 Pa	TFI DPMS
$\xi_{long.stability}$	5.0 Pa	TFI DPMS/Amb. Winds
ξ_{Patm}	118 Pa	Estimated
ξ_{msl}	0.001 kPa	Estimated
$\xi_{altitude}$	10 m	Estimated
ξ_{temp}	3 °C	Estimated
$\xi_{pressure}$	9.7 Pa	Combined
$\xi_{density}$	5.3%	Combined
ξ_{speed}	0.1 km/h	ublox GPS
ξ_{C_P}	7.0%	Combined

3. Results and discussion

In this section findings from the instrumented container are presented including a statistical analysis of the measured container pressure distributions. This is discussed in relation to variations in the pressure drag coefficient observed over the duration of the journey. Findings, over selected legs of the trip, are compared to previous studies. Finally, the observed changes in the drag coefficient are discussed in the context of variations in the natural wind environment in which experiments have been conducted.

3.1. Variation in pressure drag coefficient

We first consider how the container pressure drag coefficient varies throughout the train journey. Here we define the pressure drag coefficient:

$$C_D = \frac{\overline{P}_{front} - \overline{P}_{base}}{1/2 \cdot \rho \cdot V_T^2}, \quad (6)$$

as the difference in the area-averaged front pressure, P_{front}, and base pressure, P_{base}, represented as a force coefficient. A linear interpolation between pressure taps, that also extrapolates pressure data to container edges, has been employed when determining mean pressures coefficients. The train velocity, V_T, was obtained from the on-board GPS unit and the air density, ρ, from local weather station data.

Fig. 6(a) and Fig. 6(b) illustrates how the train velocity and the container pressure drag coefficient vary throughout the course of the journey. As the quasi-steady aerodynamic pressure force is of interest here, a rolling-average 60 s filter has been applied to the container pressure drag coefficient and is plotted on top of the raw unfiltered data. Excluding two extended periods when the train made two operational stops, the velocity was predominately above 60 km/h throughout the journey. Above this speed, the average train velocity was 96 km/h. We only consider the drag coefficient for train velocities >60 km/h to exclude operating conditions where the signal-to-noise ratio of the pressure transducers has been considered to be high. On this basis, the mean drag coefficient over the entire journey was 0.48. For an extended duration, from 0.5 h to 5.5 h, the drag coefficient remains relatively stable at 0.46 (±0.02), despite large variation in the train speed. However, after this period we observe an increase in the variability of the pressure drag coefficient, which peaks at ~0.75 and drops to ~0.35 towards the end of the trip.

To further characterise the variation in the drag coefficient over the duration of the trip, the measured time series have been analysed over discreet time periods depending on the stability and magnitude of both the train velocity and the container drag coefficient. Table 2 presents mean and unsteady statistics for five track sections of the trip that have been identified for further analysis. The location and corresponding time period of these track sections are labelled in Figs. 4 and 6 respectively. Track section 1 represents a 20 min period with high train speed and stable drag coefficient; track section 2 an extended 90 min period where the train speed is variable and the drag coefficient is relatively stable; track section 3 is similar to track section 1, but with slightly higher average train speed over the 15 min period; track sections 4 and 5 represent 10 min time periods where the highest and lowest drag coefficient values are observed over the journey for a train velocity >100 km/h.

3.2. Time-averaged analysis of surface pressures

Fig. 7 and Fig. 8 show the time-averaged front and base surface

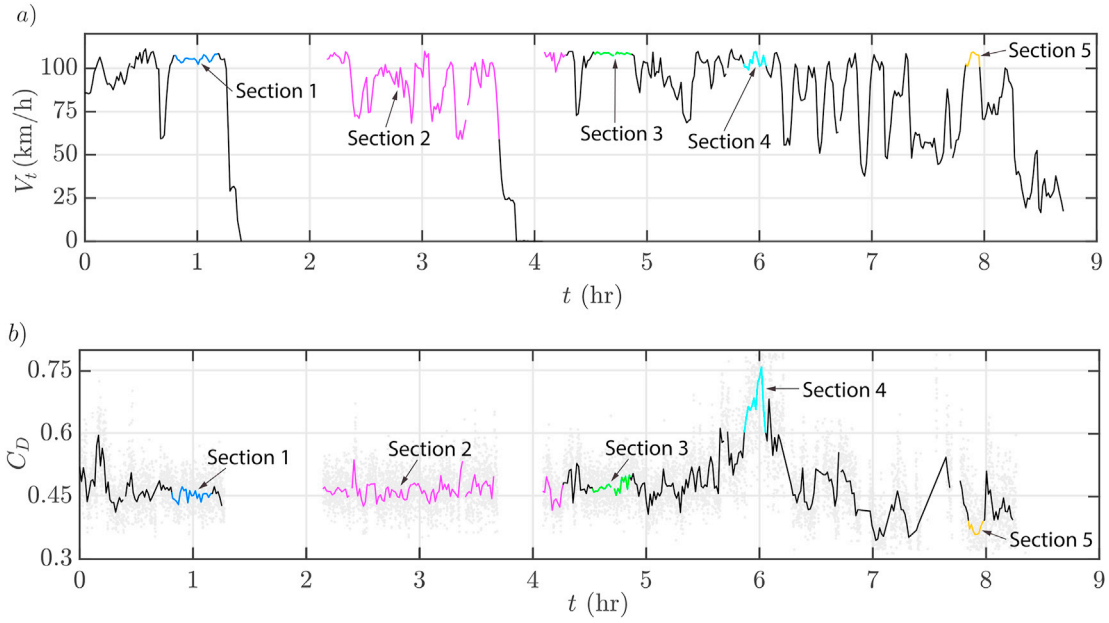

Fig. 6. a): Train velocity time series. b): Drag coefficient time series for velocities >60 km/h. Data is averaged over 60 s intervals. ● - Track section 1, ● - Track section 2, ● - Track section 3, ● - Track section 4, ● - Track section 5.

Table 2
Mean and unsteady statistics of the velocity and drag coefficient for the entire trip, and track sections 1 to 5. V_T, $\sigma(V_T)$ and C_D, $\sigma(C_D)$ are the mean and standard deviation of the train velocity and the drag coefficient, respectively. $\sigma(C_{P_{f\_taps}})$ represents the standard deviation of area-averaged pressure coefficient recorded on the front face of the container.

Track Section	Time (min)	V_T (km/h)	$\sigma(V_T)$	C_D	$\sigma(C_D)$	$\sigma(C_{P_{f\_taps}})$
Entire Trip	490	96	3.57	0.48	0.061	0.15
1	20	104	1.42	0.45	0.011	0.14
2	90	85	12.87	0.45	0.020	0.15
3	15	110	0.55	0.47	0.012	0.15
4	10	103	3.27	0.70	0.044	0.25
5	10	103	5.91	0.37	0.015	0.12

pressure contours for the entire trip, and for each of the five identified track sections. Track sections 1 to 3 are consistent with the entire trip contour, in both pressure coefficient distribution and magnitude on both the front and base surfaces. This is despite a relatively high variation in train speed observed over the duration of track section 2. Importantly, the system does not need a stable train speed to characterise quasi-steady pressure coefficients. Track section 2 results also highlight, as expected, that Reynolds number effects on force and pressure coefficients are minimal. Track section 5 results reveal a similar distribution to the entire trip time-averaged findings, however, is of a lower magnitude. One explanation for this observation is the contribution of a predicted tail-wind during this period. Track section 4 exhibits a significantly higher magnitude in the pressure drag coefficient (0.7), with the front pressure distribution being asymmetric across the vertical centre-line. This asymmetry suggests the presence of a significant cross-wind. The relatively high standard deviation in the measured surface pressures, $\sigma(C_{P_{f\_taps}})$, is also indicative of unsteady cross-wind effects. Overall the predicted local wind environment over the duration of each track section, which is discussed in detail in Section 3.4, is found to be consistent with the observed variations in the container pressure distributions and drag coefficient.

Fig. 8 shows time-averaged base pressure contours for the entire trip and track sections 1–5. Compared to the front face, the change in both the magnitude and distribution of base pressures observed throughout the journey is significantly lower. However, for track section 4 the magnitude is higher as a result of a suspected high cross-wind being present. Changes in the time-averaged base pressure coefficients across each track section contributes to <4% of the measured variation in the drag coefficient across each of the identified track sections. The range in the magnitude of base pressure coefficients across all track sections is of the order of 0.05. This is lower than base pressure ranges reported by previous wind tunnel and numerical studies which report ranges of the order of −0.2 (Li et al., 2017; Maleki et al., 2019).

3.3. Comparison of drag coefficient and pressure distribution to previous studies

In this section we compare the time-averaged field results to past work. Table 3 presents both experimental and numerical work completed on the aerodynamics of train geometries. The studies report on the aerodynamic drag coefficient of containers and carriages and have been ordered from high to low drag so that they may be compared with the current study results. Compared to the isolated container studies (Östh and Krajnović, 2014; Li et al., 2015; Maleki et al., 2017), the field C_D finding is ∼ 50% lower. Studies that report similar, or lower C_D values to the present study, have been conducted for much smaller gap sizes (Gielow and Furlong, 1988; Soper, 2016; Engdahl et al., 1987). These investigations have been conducted for gap sizes $0.44W$–$4.60W$, where shielding from the upstream container would be expected to have a significant effect and account for the low C_D values reported. Studies with a comparable gap size (Li et al., 2017; Maleki et al., 2019) have reported relatively stable C_D values with respect to increasing gap size, note C_D values that are ∼ 55%–75% higher than findings from the field.

The key difference between all of these past investigations and the current study is the instrumented container is located significantly further downstream from the leading upstream body. This is indicative of the difference in the magnitude of the Reynolds number, Re_L, between studies, where the characteristic length scale is based on the distance between the front of the train to the instrumented container. Engdahl et al. (1987) has also conducted field based measurements on the aerodynamic drag of containers for operational Reynolds numbers, however, the gap size between adjacent containers in this study was very low ($0.44W$). The majority of investigations that report C_D findings of containers have been conducted at a Re_L of the order of 10^6 whereas the

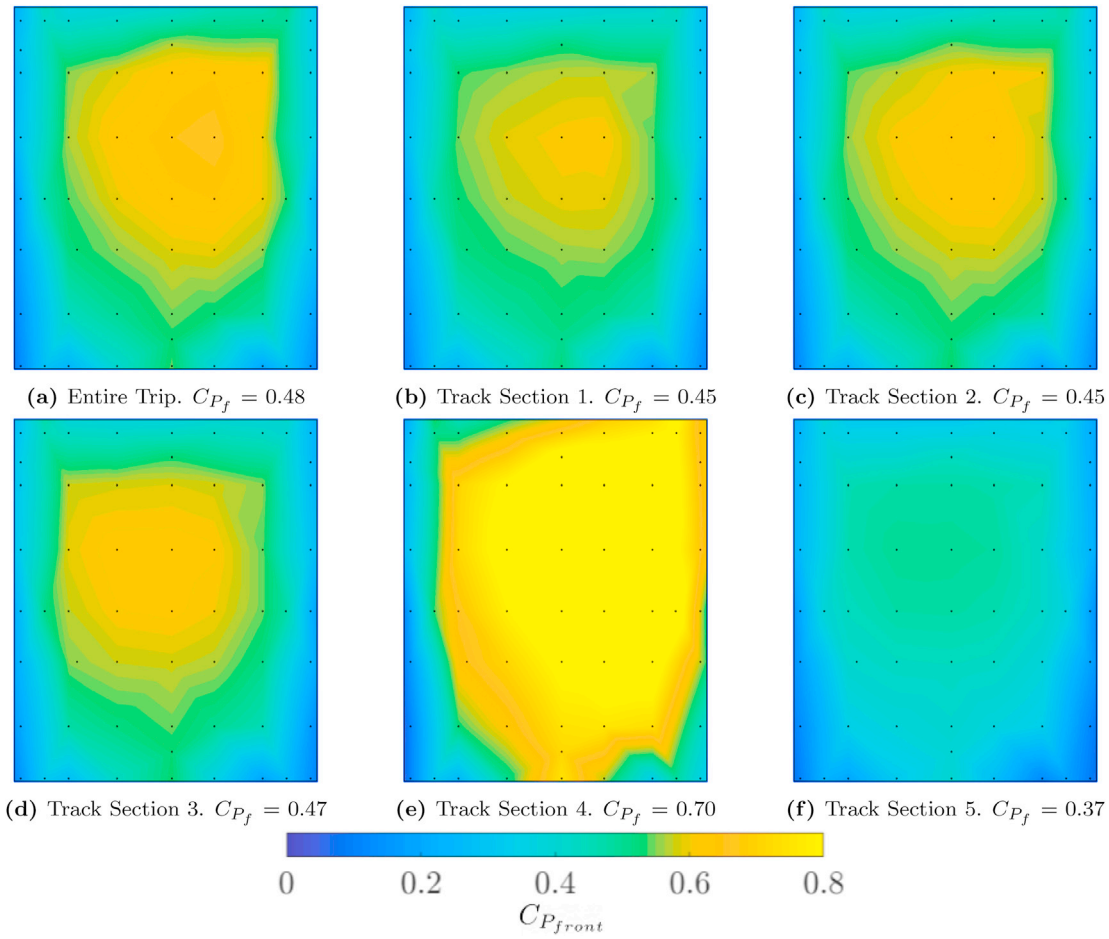

Fig. 7. a): Mean pressure coefficient of the front surface over the entire trip. b)–f): Mean pressure coefficient of track sections 1–5. The z and y axes are normalised by the height and width of the container respectively.

current study is representative of a Re_L of the order of 10^8. This difference, and secondary effects arising from variations in geometry and a moving ground plane, may suggest that current investigations are yet to completely detail the drag profile of long trains. This is also supported by recent investigations by Bell et al. (2020), who detailed the growth rate of the boundary layer along the length of full-scale operational freight trains. Their findings show that a high growth rate region of the boundary layer may be expected over the first ~ 200 m of operational freight train configurations. The aerodynamic loading on containers would also be expected to vary significantly in high growth rate areas of the boundary layer. To date both wind tunnel and numerical studies have not considered such large length scales for the container gap sizes investigated here.

Despite these differences, field pressure distributions are found to compare well with what might be expected based on the findings of Li et al. (2017) and Maleki et al. (2019). These studies represent the closest test conditions compared to the field results. Fig. 9 compares pressure distributions for the front surface of the container for these and the current study. Here, the distributions have been normalised by the maximum pressure coefficient of the front $\max(C_{P_f})$ so that only the shape of the distributions may be compared. Despite differences in aspect ratio of the loading configuration between the studies compared, which is expected to have minimal impact on pressure distributions for the range of aspect ratios considered here (Martinuzzi and Tropea, 1993), the general shape of the distributions is similar. The highest stagnation pressure occurs on the top half of the container and then decreases rapidly towards the edges for all studies. This is also consistent with Östh and Krajnović (2014) for a single-stacked train.

3.4. Relationship between remote wind data and drag coefficient

The following sections are dedicated to providing additional insight into the variation in the container measurements observed throughout this field-study. This is achieved through analysing the variation in the pressure drag coefficient with changes in the container pressure distributions and weather conditions observed throughout the journey. As indicated in the previous sections, the natural wind environment has a clear impact on container surface pressures in addition to the train motion. In the absence of direct knowledge of the local weather conditions at the track, we compare container measurements with data sets originating from Australian Bureau of Meteorology (BoM) weather stations located close to the train route. It is acknowledged that the wind environment measured at these stations will differ from local conditions experienced by the train. Here we show that the time-averaged weather station wind statistics over the duration of each track section to be consistent with the observed variations in the container pressure distributions and drag coefficient.

Table 4 provides a summary of the nearest weather station data for each track section, where X_{WS} represents the maximum distance from the weather station to the track section. The BoM wind speed, V_w and direction, φ_w data sets represent the time-averaged conditions over the duration of each track section. Wind velocity measurements at the BoM sites are taken at 10 m from the ground. These measurements have been adjusted to reflect wind conditions at a height of 3 m, the height of the train, using a logarithmic atmospheric boundary layer profile with an exponent of 0.06. Measured wind angles and velocities are defined in Fig. 10 and have been used to derive the predicted wind yaw angle, θ_{yaw},

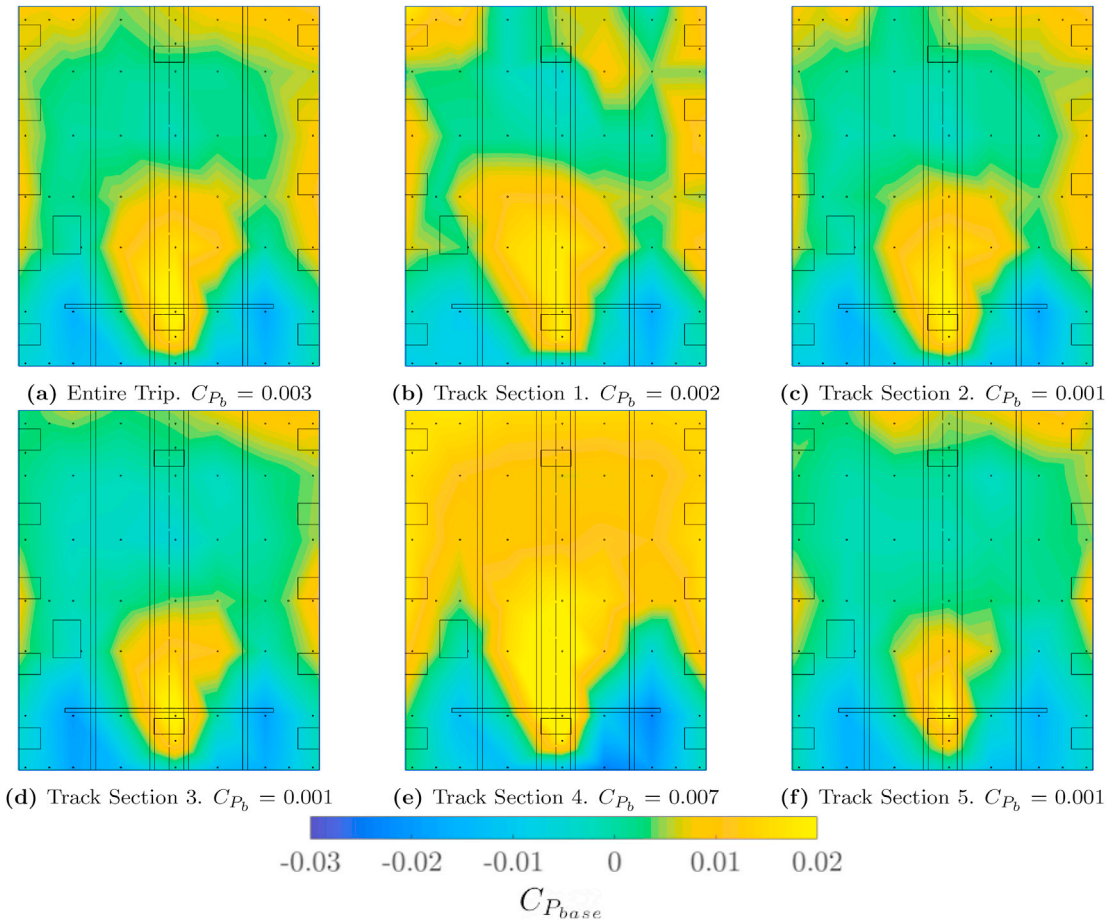

Fig. 8. a): Mean pressure coefficient of the base surface of entire trip; b)–f): Track sections 1–5 from left to right. The z and y axes are normalised by the height and width of the container respectively.

Table 3
Summary of pressure drag coefficients and test setups from past studies. Here, Re_L is the Reynolds number based on the distance from the front of the train to the instrumented container.

	Test	AspectRatio	No.upstream	FrontGap	BaseGap				
Study	Method	(H/W)	gaps	(W)	(W)	Re_L	C_{P_f}	C_{P_b}	C_D
Li et al. (2015)	Wind tunnel	2.56	0	∞	∞	–	0.74	−0.20	0.94
Maleki et al. (2017)	Wind tunnel	2.56	0	∞	∞	–	0.73	−0.20	0.93
Östh and Krajnović (2014)	Numerical	1.60	0	∞	∞	–	–	–	0.90
Li et al. (2017)	Wind tunnel	2.56	2	12.60	12.6	1.5×10^6	0.59	−0.20	0.79
Maleki et al. (2019)	Numerical	2.56	2	6.50	0.30	1.5×10^6	0.56	−0.13	0.69
Gielow and Furlong (1988)	Wind tunnel	1.02	1	4.60	0.6	8.31×10^7	–	–	0.55
Soper (2016)	Moving-model	1.02	2	4.60	0.65	1.41×10^6	–	–	0.46
Current	Full-scale	1.18	7	13.6	13.60	3.7×10^8	0.45	0.00	0.45
Engdahl et al. (1987)	Full-scale	1.08	7	0.44	0.3	3.61×10^8	–	–	0.30

experienced by the train. Here, the train velocity is defined by V_T, the train direction of travel is defined by the heading angle measured from the true North, φ_T, the air velocity experienced by the train due to its motion by V_t, and V_r represents the relative wind velocity.

Using data obtained from the BoM weather station sites, early investigations attempted to analyse the drag coefficient in terms of the relative wind speed experienced by the container. This approach was found to introduced more variation into the drag coefficient compared to using the train ground speed as the reference variable and was ultimately deemed unsuccessful. An improved correlation with the variation in the drag coefficient throughout the track sections was made with the time-averaged wind speed and direction throughout the duration of each track section. To this extent, in Table 4, we have categorised the general nature of the wind conditions into low-wind, cross-wind and tail-wind conditions experienced by the train. Although the exact nature of the atmospheric wind conditions at the train is unknown, low-wind conditions are generally consistent with nearby weather stations recording wind speeds <10 km/h.

Track sections 1–3 are characteristic of low-wind conditions where a relatively stable drag coefficient throughout each section was observed. Track section 1 provided the most stable drag coefficient. Over this section a westerly wind of 2.9 km/h was recorded and the estimated yaw angle is 1.4°. The largest distance from a weather station to the train over this track section is 21.2 km. In contrast to this, the largest distance between the train and a weather station over track section 2, 112 km, is much greater as a result of the longer track section length. Hence the predicted yaw angle of 2.8°, over such as large track section, may not be completely representative of the local time-averaged conditions. Wind

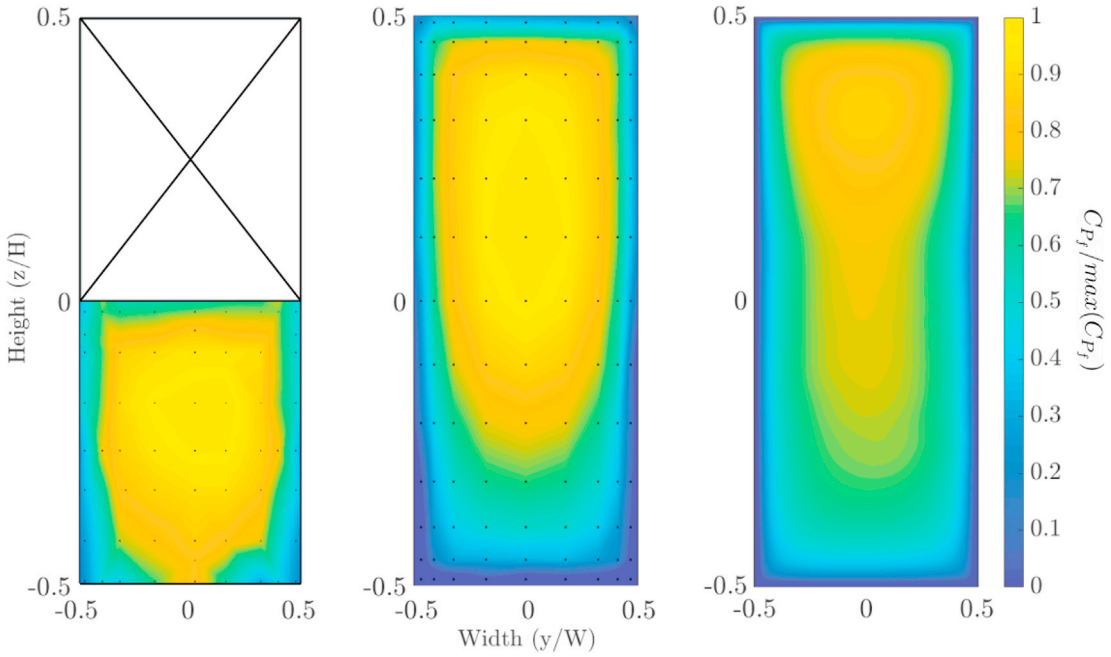

Fig. 9. Pressure coefficient distribution normalised to maximum value of each distribution. Left to right: single-stacked (this study); double-stacked wind tunnel Li et al. (2017); double-stacked numerical simulation (Maleki et al., 2017).

Table 4
Summary of weather station data at sites nearest to track sections 1 to 5. Here, X_{WS} is the distance from the weather station to the track.

Parameters	Tracksection 1	Tracksection 2	Tracksection 3	Tracksection 4	Tracksection 5
Closest weather station	Keith	Nhill/Horesham	Stawell	Westmere	Avalon
Altitude (m)	27	139/134	235	226	11
Max. X_{WS} (km)	21	112	43	5	21
T (°C)	16.9	19.6	17.9	15.0	21.8
ρ (kg/m^3)	1.22	1.19	1.18	1.20	1.20
C_{P_a}	−0.048	−0.003	−0.045	−0.200	−0.012
V_w (km/h) and φ_w	2.9 W	5.8 SE	8.6 S	10.8 SW	6.7 WNW
V_T (km/h) and φ_T	104 SE	85 W	110 SSE	103 SE	103 ENE
V_r (km/h)	102.8	89.1	115.9	103.0	98.4
θ_{yaw} (°)	1.5	2.8	1.6	6.0	2.7
Identified wind type	Low	Low	Low	Cross	Tail
C_D	0.45	0.45	0.47	0.70	0.37

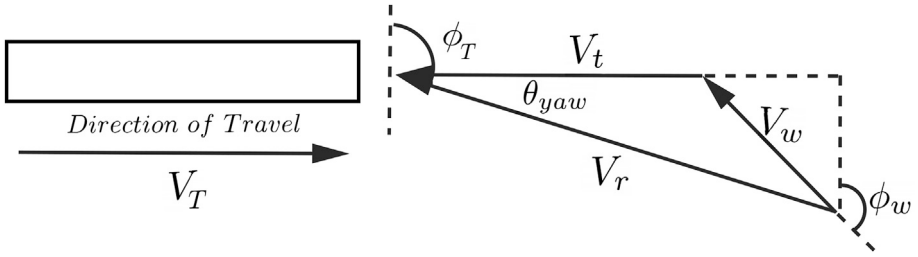

Fig. 10. Velocity vector diagram and definitions. Here φ_w is defined relative to the wind direction and φ_T is the measure from true North.

conditions measured during section 3 suggest that the train may have experienced a slight head-wind at times during this section. This is also consistent with the slightly higher drag coefficient (0.47) measured over this section of track compared to sections 1 and 2.

Unlike the low-wind conditions, during track sections 4 and 5 significant variations in the drag coefficient from the entire trip average were observed. The highest wind speeds and estimated yaw angle occurred during track section 4. As expected the largest drag coefficient and level of asymmetry was observed during this track section throughout the entire trip The largest drag coefficient and level of asymmetry in the measured pressure distributions was also observed during this section. Compared to track section 1, the drag coefficient and the time averaged weather station yaw estimate is found to increase by 0.25 and 4.5° respectively. Finally track section 5 has a moderately high tail-wind resulting in the predicted train air speed being 5 km/h lower than the train ground speed. This predicted velocity offset can partially account for the difference in the drag coefficient between the low-wind (0.45) and tail-wind conditions (0.37).

To further describe variations in container measurements, both within and between each track sections, probability distributions of the

drag coefficient are plotted in Fig. 11 for the entire trip and each track section. Probability distributions have been compiled using raw data sets for train speeds >60 km/h. The probability distributions are shown in the standardised format with the random variable represented in the reduced form with zero mean and unitary standard deviation. Bin sizes for each distribution have been scaled based on the square-root of the number of samples recorded for each track section analysed. The probability distribution of the drag coefficient over the entire trip exhibits skewed and leptokurtic behaviour. A Normal distribution, with 0.7σ, is overlaid over the entire trip data-set to demonstrate this. This behaviour is expected since for the majority of the trip a steady drag coefficient was observed with relatively short time periods of extreme low and high values. The skewed nature of the distribution is characteristic of the natural wind environment effect on the measured pressure distributions.

For the predicted low-wind conditions, the drag coefficient measured during track sections 1–3 is reasonably well represented by a standard normal distribution. Track section 2 provides the best fit to the standard normal distribution as this section experienced stable wind conditions for the largest time period where pressure fluctuations are expected to be normally distributed. The lowest variance in the drag coefficient was measured over this track section compared to all others. For track section 4, where a mean cross-wind is predicted, the distribution is positively skewed since there are more extreme positive peaks in the drag coefficient. For the tail-wind case of track section 5, a Rayleigh distribution provides a better fit to the data compared to a normal distribution. When predicting wind speeds in a turbulent atmospheric boundary layer a Raleigh distribution is often used (Justus et al., 1976). The trend suggests that the pressure signature, resulting from the unsteady natural wind environment, is being observed in the surface pressure data.

3.5. Relationship between pressure distribution asymmetry, drag coefficient and yaw

Throughout the journey the wind effect on container measurements has been described. The variation in the surface pressure distributions, which include both pressure magnitudes and asymmetry levels, are in broad agreement with what one may expect given the remote weather station data. Particularly over track section 4, where the largest cross-winds are expected, an increase in the drag coefficient and the level of asymmetry of the surface pressure distributions was found. To gain further insight into the prevalence of cross-winds over the entire trip, an asymmetry measure (C_{P_α}) was defined:

$$C_{P_\alpha} = C_{P_{front,left}} - C_{P_{front,right}}, \tag{7}$$

as a proxy for the magnitude of the cross-wind component experienced by the train, where C_{P_α} is the difference in the pressure coefficients averaged over the vertical left, $C_{P_{front,left}}$, and right, $C_{P_{front,right}}$, halves of the front surface. The asymmetry measure was determined over the length of the trip and the time series is plotted in Fig. 12. For the majority of the

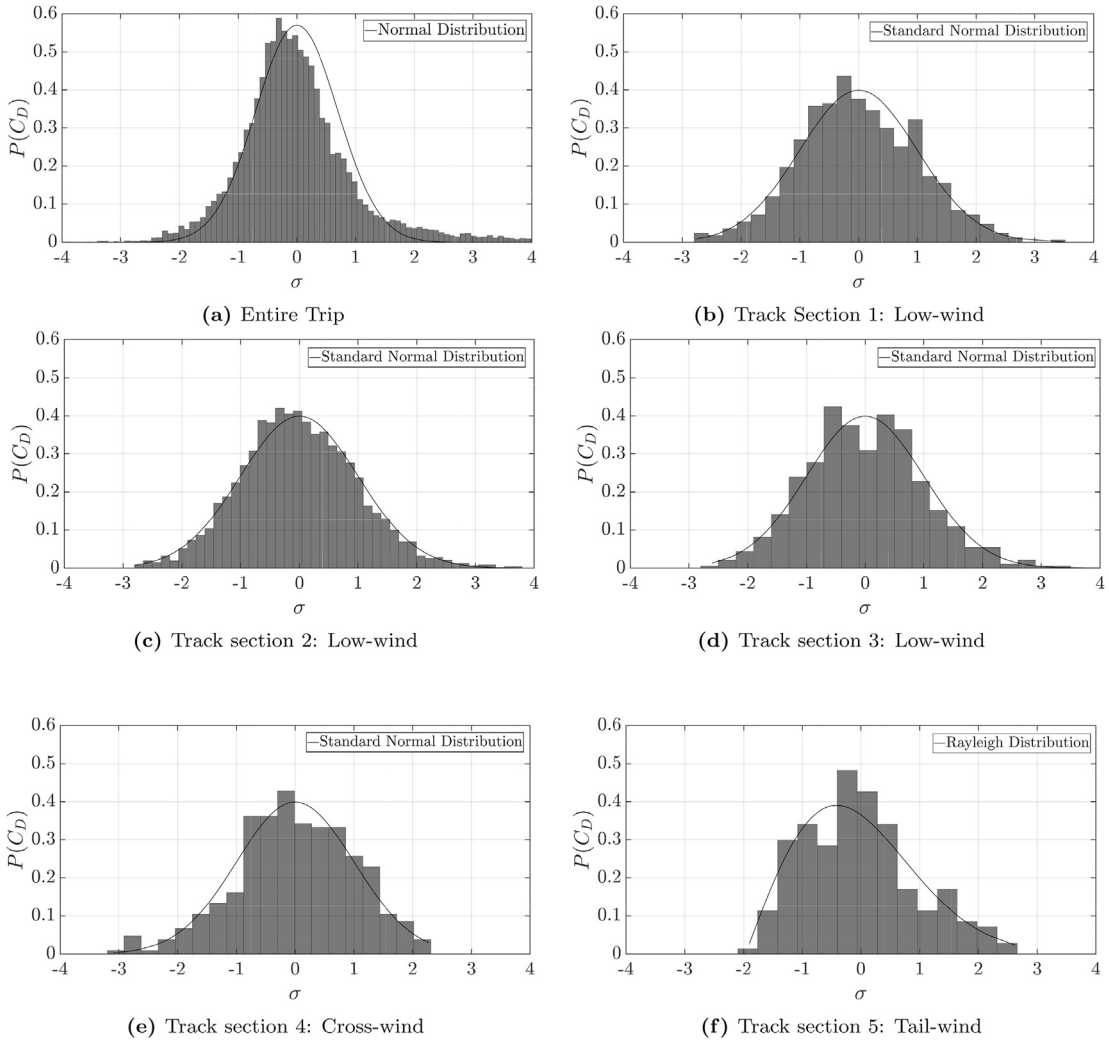

(a) Entire Trip
(b) Track Section 1: Low-wind
(c) Track section 2: Low-wind
(d) Track section 3: Low-wind
(e) Track section 4: Cross-wind
(f) Track section 5: Tail-wind

Fig. 11. Drag coefficient probability density distributions for the entire trip and track section 1–5.

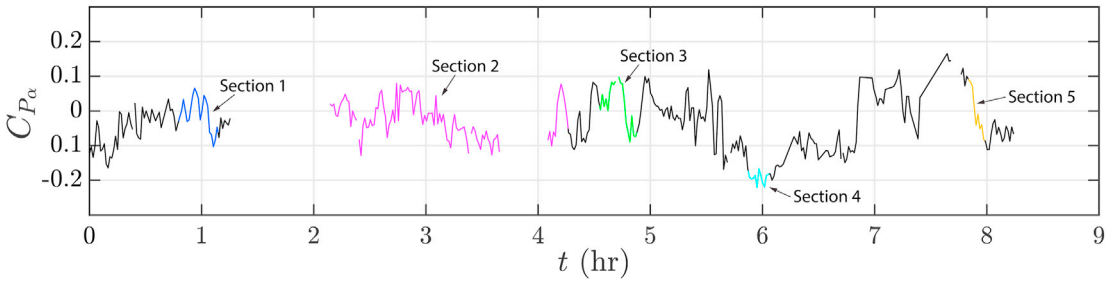

Fig. 12. Time series of C_{P_α} over the entire trip. ● - Track section 1, ● - Track section 2, ● - Track section 3, ● - Track section 4, ● - Track section 5.

trip C_{P_α} varied between ±0.1, excluding the period where the drag coefficient was seen to peak in track section 4, and a short period (also associated with an increased drag coefficient) in the first hour of the trip. When the drag coefficient is stable, over track sections 1–3, the asymmetry measure is observed to vary between ±0.1. Outside this range may be an indicator of higher wind yaw angles being present.

To determine if any robust relationships can be drawn between increased drag and asymmetry, the absolute value of C_{P_α} was plotted against pressure drag coefficient, as presented in Fig. 13. Each data point represents a 60 s average of the raw data. The variation in the drag coefficient with the asymmetry measure is consistent with the predicted prevailing wind conditions throughout the trip. This is highlighted in 13 for track sections 1, 4 and 5. Track sections 2 and 3, which are considered a low-wind case with track section 1, are not shown for clarity. Track section 1 is predicted to represent a low-wind case, track section 4 a cross-wind case and track section 5 a tail-wind case. In general, when a low-wind case is observed the C_{P_α} value is below 0.05 with the standard deviation of the drag coefficient being ~ 0.04. In this range the drag remains relatively constant with the absolute value of C_{P_α}. Once the asymmetry increases and a proposed cross-wind is predicted the drag coefficient increases with the square of C_{P_α}. A quadratic function least squares fit has been applied to the data from a C_{P_α} value > 0.05 where the R-squared coefficient is 0.7 and a constant drag coefficient of 0.44 below this.

In order to establish a yaw angle estimate for the field study, a relationship connecting the C_{P_α} measure to the wind yaw angle is required. Here, we establish this relationship based on the computational study of Maleki et al. (2020), who used the Shear-Stress Transport (SST) Improved Delayed Detached Eddy Simulation (IDDES) methodology to predict the drag on containers. Through their simulations, the aerodynamics of freight train containers under yawed flow conditions, for a range of front and base gap sizes, was investigated. Fig. 14 presents the relationship between C_{P_α} and yaw angle based on the simulated container surface pressure field results at yaw. This relationship has been established for the largest gap size simulated (6.46W), where, as expected in this study, the dependence of the drag coefficient on the front gap size was weak. For the yaw angle range of relevance here an approximately linear relationship:

$$\theta_{yaw} = 62.3 \cdot C_{P_\alpha}, \tag{8}$$

Exists between the asymmetry measure and yaw angle, where the R-squared coefficient is 0.97. This result is also consistent with the findings of Gallagher et al. (2018), who has also employed a similar method to that described here to estimate yawed flow conditions experienced by trains.

Fig. 15 collates findings from a number of previous studies who report on the change in drag coefficient of train containers and carriages with yaw angle. These results are compared to the instrumented container findings using equation (8) to derive a yaw angle estimate for the present study. Results from previous studies span a range of test configurations

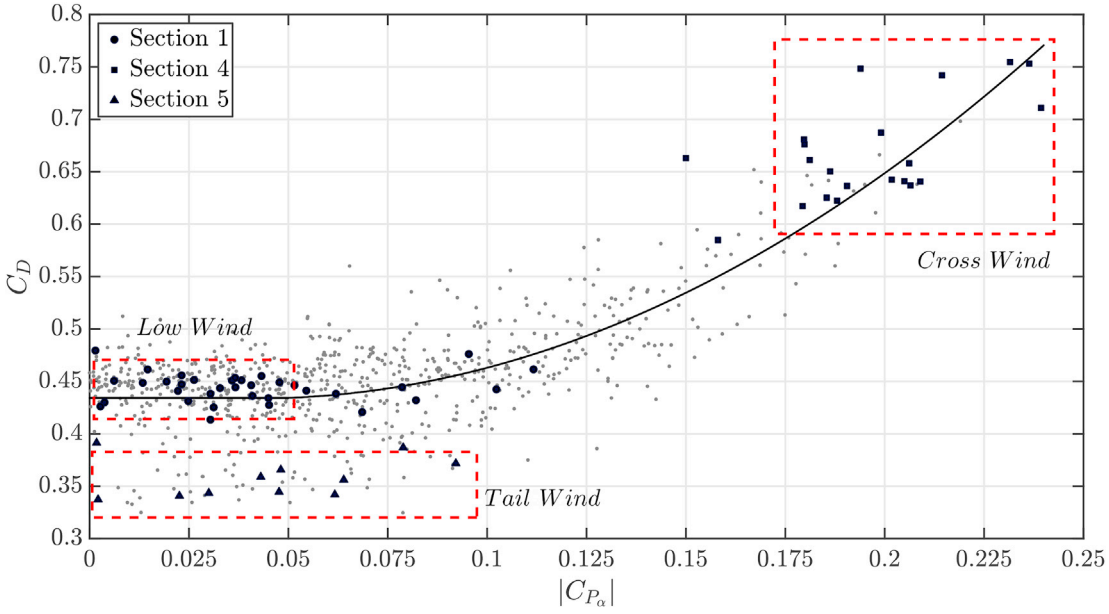

Fig. 13. Variation of drag coefficient with asymmetry measure ($|C_{P_\alpha}|$), highlighting results for track sections 1, 4, and 5, corresponding to different wind conditions. The whole data-set is shown as grey symbols. The black line represents the best-fit trend-line.

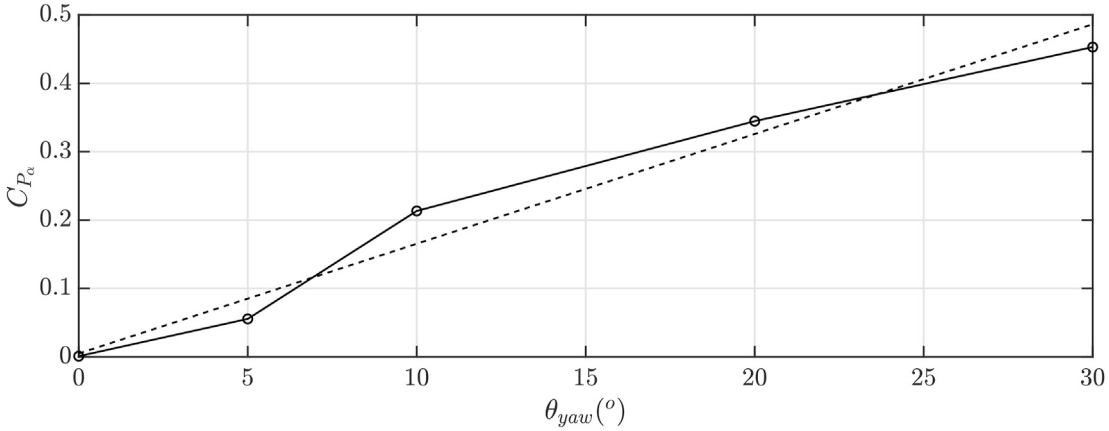

Fig. 14. Approximate linear relationship of θ_{yaw} with C_{P_a} (dotted line) reprocessed from Maleki et al. (2020) for a double-stacked train. The numerical predictions of Maleki et al. (2020) are shown by the symbols with the solid lines providing a guide.

and train geometries, that include; isolated container cases (Beagles and Fletcher, 2013; Watkins et al., 1992) to relatively small gap sizes 0.3*W*–0.5*W* (Watkins et al., 1992; Golovanevskiy et al., 2012) to relatively large gap sizes 5.5*W*–6.5*W* (Giappino et al., 2018; Maleki et al., 2020). In contrast to the present investigation all of these studies have been preformed with the instrumented container located close to the front of the train. Despite the differences in test set-up however, the relationship established between the ΔC_D and yaw angle for this investigation is found to lie in-between the trends established from past studies.

For the cross-wind case identified in this study, a time-average yaw angle of ~12° is estimated through employing equation (8). We note that the time-averaged yaw angle determined from remote weather station data during this period was 6°. We note that this difference is most likely indicative of the limitations of using the remote weather station data to provide an accurate prediction of the local wind conditions experienced by the train and the method used to establish the relationship between C_{P_a} and yaw for the present study. In future studies we plan to establish a stronger relationship between the estimated yaw angle and C_{P_a} through controlled wind tunnel experiments and also via track side measurements of the wind conditions experienced trains loaded with the instrumented container.

4. Conclusion

A novel field study was employed where a full-scale shipping container was pressure tapped with a total of 118 taps on the front and rear surfaces, and placed on a freight train that travelled over 700 km at an average speed at 95 km/h. This work represents a rare field study that demonstrates an empirical method for determining surface pressure distributions and pressure drag on a intermodal shipping container under natural environmental conditions. The methodology was shown to produce self-consistent data for train speeds above 60 km/h even for moderate variations in ambient wind conditions. For the case examined, the instrumented container was positioned 185 m from the nose of the train, with significant upstream and downstream inter-container gaps of 13.6 wagon widths, thus representing a moderately isolated container positioned within a relatively well developed train boundary layer. Previous full-scale force balance studies (Engdahl et al., 1987) have indicated that the drag on each wagon begins to stabilise after 160 m from the second

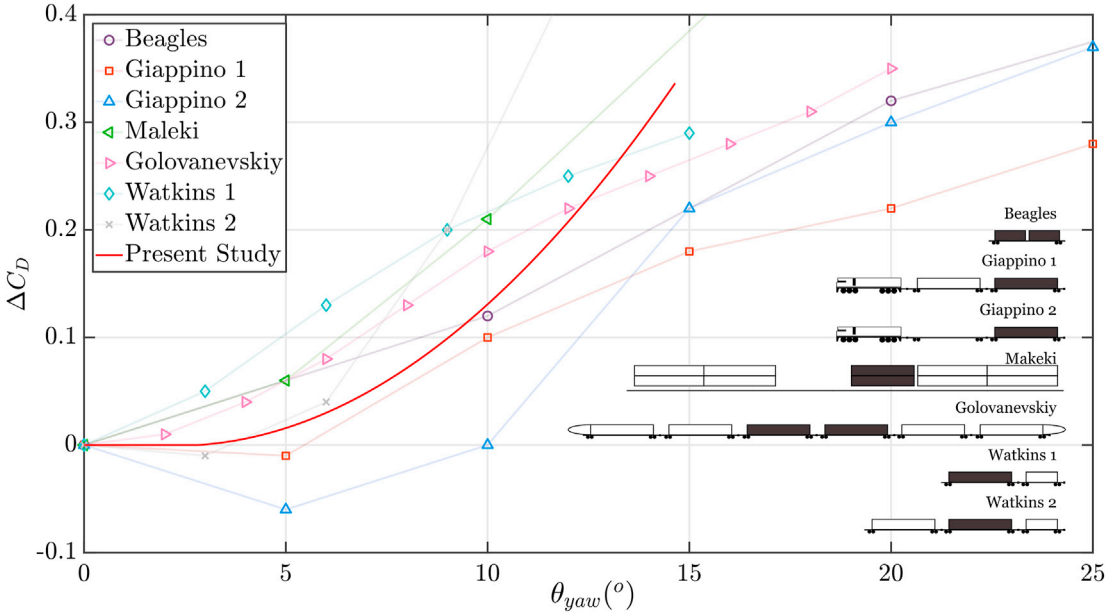

Fig. 15. Change in the drag coefficient (ΔC_D) against yaw angle from the following studies: Beagles and Fletcher (2013); Giappino et al. (2018); Golovanevskiy et al. (2012); Watkins et al. (1992); Maleki et al. (2020), together with the trend found in the present study.

wagon. Further to this recent full-scale field studies (Bell et al., 2020) and scale-model wind-tunnel studies (Soper et al., 2014) have indicated that the train boundary layer begins to stabilise 200 m and 100 m respectively from the nose of the train. This suggests that the predicted drag and its variation with yaw may for the present work may be generally representative of (relatively isolated) containers spanning the majority of a typical train length (1–2 km).

Five distinct periods were identified throughout the trip that were characteristic of different operational conditions. Three of these included: a section of track where the pressure drag coefficient had small variance; a track section where the drag peaked to a maximum; and finally a track section where the time-averaged track-section drag was considerably lower. For steady low-wind conditions (<10 km/h) the measured pressure drag coefficient was 0.45. The general distributions of front and rear surface pressures obtained under low-wind conditions were consistent with those found in recent wind-tunnel experiments and flow simulations; however, the magnitude of the pressure drag coefficient was found to be ~ 65% lower in comparison. A primary difference between the current and previous studies is that the case examined here is for an instrumented container positioned at a relatively larger distance downstream from the start of the train. This suggests that past studies may not have been able to capture the complete variation of drag on containers over the entire length of long freight trains.

Throughout the train journey periods of high asymmetry in the frontal surface pressure distributions were observed. These were found to be consistent with cross-wind conditions and higher pressure drag coefficients. An asymmetry measure was established, as a proxy for the wind yaw angle, and a relationship was drawn between the pressure drag coefficient and this measure. In particular, an approximate quadratic variation was observed between the pressure drag coefficient difference from the zero yaw case and the asymmetry. The highest drag coefficient measured for the predicted largest cross wind case corresponds to similar drag coefficient values that have been reported in previous studies for low yawed flow test conditions.

Based on the analysis of predictions from a previous numerical investigation, an approximately linear relationship was found between the wind yaw angle and the asymmetry measure. For low yaw angles (<10%), the variation of drag coefficient with the yaw angle estimate obtained in the study is in broad agreement with the general spread to drag coefficients reported in literature for train containers at yaw, noting that the published cases cover a wide range of different setups. While further work is required to characterise the effect of upstream and downstream gap size, container position along the train, and varying wind conditions, this study can provide a degree of confidence that the testing methodology employed can be a useful tool to understand the aerodynamics of freight trains in the field.

CRediT authorship contribution statement

Ariq Quazi: Conceptualization, Methodology, Software, Validation, Formal analysis, Investigation, Data curation, Writing - original draft, Visualization, Project administration. **Timothy Crouch:** Conceptualization, Methodology, Writing - review & editing, Supervision, Project administration. **James Bell:** Conceptualization, Methodology, Software, Validation, Writing - review & editing, Project administration, Funding acquisition. **Tony McGreevy:** Resources, Funding acquisition. **Mark C. Thompson:** Conceptualization, Supervision, Writing - review & editing, Funding acquisition. **David Burton:** Conceptualization, Methodology, Supervision, Writing - review & editing, Resources, Project administration, Funding acquisition.

Declaration of competing interest

The authors declare that they have no known competing financial interests or personal relationships that could have appeared to influence the work reported in this paper.

Acknowledgement

This research was supported through Pacific National Rail and the Australian Research Council's Linkage Project funding scheme, under project number LP13100953.

References

Baker, C., 2010. The simulation of unsteady aerodynamic cross wind forces on trains. J. Wind Eng. Ind. Aerod. 98 (2), 88–99.
Baker, C.J., Sterling, M., 2009. Aerodynamic forces on multiple unit trains in cross winds. J. Fluid Eng. 131 (10).
Baker, C.J., Quinn, A., Sima, M., Hoefener, L., Licciardello, R., 2014. Full-scale measurement and analysis of train slipstreams and wakes. part 1: ensemble averages. Proc. Inst. Mech. Eng. - Part F J. Rail Rapid Transit 228 (5), 451–467.
Beagles, A.E., Fletcher, D.I., 2013. The aerodynamics of freight: approaches to save fuel by optimising the utilisation of container trains. Proc. Inst. Mech. Eng. - Part F J. Rail Rapid Transit 227 (6), 635–643.
Bell, J., Burton, D., Thompson, M., 2020. The boundary-layer characteristics and unsteady flow topology of full-scale operational inter-modal freight trains. J. Wind Eng. Ind. Aerod. 201, 104164.
Copley, J., 1987. The three-dimensional flow around railway trains. J. Wind Eng. Ind. Aerod. 26 (1), 21–52.
Davis, W.J., 1926. The Tractive Resistance of Electric Locomotives and Cars. General Electric.
Engdahl, R., Gielow, R., Paul, J., 1987. Train resistance-aerodynamics: volume i of ii. intermodal car application. In: Railroad Energy Technology Conference II (1986).
Flynn, D., Hemida, H., Soper, D., Baker, C., 2014. Detached-eddy simulation of the slipstream of an operational freight train. J. Wind Eng. Ind. Aerod. 132, 1–12.
Flynn, D., Hemida, H., Baker, C., 2016. On the effect of crosswinds on the slipstream of a freight train and associated effects. J. Wind Eng. Ind. Aerod. 156, 14–28.
Gallagher, M., Morden, J., Baker, C., Soper, D., Quinn, A., Hemida, H., Sterling, M., 2018. Trains in crosswinds–comparison of full-scale on-train measurements, physical model tests and cfd calculations. J. Wind Eng. Ind. Aerod. 175, 428–444.
Giappino, S., Melzi, S., Tomasini, G., 2018. High-speed freight trains for intermodal transportation: wind tunnel study on the aerodynamic coefficients of container wagons. J. Wind Eng. Ind. Aerod. 175, 111–119.
Gielow, M., Furlong, C., 1988. Results of wind tunnel and full-scale tests conducted from 1983 to 1987 in support of the association of american railroads' train energy program. Technical report (No. AAR R-685).
Golovanevskiy, V.A., Chmovzh, V.V., Girka, Y.V., 2012. On the optimal model configuration for aerodynamic modeling of open cargo railway train. J. Wind Eng. Ind. Aerod. 107–108, 131–139.
Hemida, H., Krajnović, S., 2010. LES study of the influence of the nose shape and yaw angles on flow structures around trains. J. Wind Eng. Ind. Aerod. 98 (1), 34–46.
Holman, J., 2012. Experimental Methods for Engineers, eighth ed.
Justus, C., Hargraves, W., Yalcin, A., 1976. Nationwide assessment of potential output from wind-powered generators. J. Appl. Meteorol. 15 (7), 673–678.
Krajnović, S., Ringqvist, P., Nakade, K., Basara, B., 2012. Large eddy simulation of the flow around a simplified train moving through a crosswind flow. J. Wind Eng. Ind. Aerod. 110, 86–99.
Lai, Y.-C., Barkan, C.P., Önal, H., 2008. Optimizing the aerodynamic efficiency of intermodal freight trains. Transport. Res. E Logist. Transport. Rev. 44 (5), 820–834.
Li, C., Kost, M., Burton, D., Sheridan, J., Thompson, M.C., 2015. Wind tunnel investigation of a double stacked wagon in free-stream. In: ASME/JSME/KSME 2015 Joint Fluids Engineering Conference. American Society of Mechanical Engineers Digital Collection.
Li, C., Burton, D., Kost, M., Sheridan, J., Thompson, M.C., 2017. Flow topology of a container train wagon subjected to varying local loading configurations. J. Wind Eng. Ind. Aerod. 169, 12–29.
Maleki, S., Burton, D., Thompson, M.C., 2017. Assessment of various turbulence models (ELES, SAS, URANS and RANS) for predicting the aerodynamics of freight train container wagons. J. Wind Eng. Ind. Aerod. 170, 68–80.
Maleki, S., Burton, D., Thompson, M.C., 2019. Flow structure between freight train containers with implications for aerodynamic drag. J. Wind Eng. Ind. Aerod. 188, 194–206.
Maleki, S., Burton, D., Thompson, M.C., 2020. On the flow past and forces on double-stacked wagons within a freight train under cross-wind. J. Wind Eng. Ind. Aerod. (in press).
Martinuzzi, R., Tropea, C., 1993. The flow around surface-mounted, prismatic obstacles placed in a fully developed channel flow (data bank contribution). J. Fluid Eng. 115 (1), 85–92.
Östh, J., Krajnović, S., 2014. A study of the aerodynamics of a generic container freight wagon using large-eddy simulation. J. Fluid Struct. 44, 31–51.
Quinn, A., Sterling, M., Robertson, A., Baker, C., 2007. An investigation of the wind-induced rolling moment on a commercial vehicle in the atmospheric boundary layer. Proc. Inst. Mech. Eng. - Part D J. Automob. Eng. 221 (11), 1367–1379.
Richardson, G., Hoxey, R., Robertson, A., Short, J., 1997. The silsoe structures building: comparisons of pressures measured at full scale and in two wind tunnels. J. Wind Eng. Ind. Aerod. 72, 187–197.
Soper, D., 2016. The Aerodynamics of a Container Freight Train. Springer.
Soper, D., Baker, C., Sterling, M., 2014. Experimental investigation of the slipstream development around a container freight train using a moving model facility. J. Wind Eng. Ind. Aerod. 135, 105–117.

Soper, D., Baker, C., Sterling, M., 2015. An experimental investigation to assess the influence of container loading configuration on the effects of a crosswind on a container freight train. J. Wind Eng. Ind. Aerod. 145, 304–317.
Sterling, M., Baker, C.J., Jordan, S.C., Johnson, T., 2008. A study of the slipstreams of high-speed passenger trains and freight trains. Proc. Inst. Mech. Eng. - Part F J. Rail Rapid Transit 222 (2), 177–193.
Surry, D., 1991. Pressure measurements on the Texas tech building: wind tunnel measurements and comparisons with full scale. J. Wind Eng. Ind. Aerod. 38 (2–3), 235–247.
Taylor, Z.J., Palombi, E., Gurka, R., Kopp, G.A., 2011. Features of the turbulent flow around symmetric elongated bluff bodies. J. Fluid Struct. 27 (2), 250–265.
ublox, 2012. MAX-6 u-blox 6 GPS modules data sheet. Preliminary 6.
Uystepruyst, D., Krajnović, S., 2013. LES of the flow around several cuboids in a row. Int. J. Heat Fluid Flow 44, 414–424.
Watkins, S., Saunders, J., Kumar, H., 1992. Aerodynamic drag reduction of goods trains. J. Wind Eng. Ind. Aerod. 40 (2), 147–178.